Lawrence Berkeley National Laboratory

Title

Correlative analysis of structure and chemistry of LixFePO4 platelets using 4D-STEM and X-ray ptychography

Permalink

https://escholarship.org/uc/item/76g3h32p

Authors

Hughes, LA
Savitzky, Benjamin H
Deng, Haitao D
et al.

Publication Date

2022

DOI

10.1016/j.mattod.2021.10.031

Copyright Information

Peer reviewed

Correlative analysis of structure and chemistry of Li$_x$FePO$_4$ platelets using 4D-STEM and X-ray ptychography

L.A. Hughes [1,#,*], Benjamin H. Savitzky [1,#], Haitao D. Deng [2,#], Norman L. Jin [2], Eder G. Lomeli [2], Young-Sang Yu [3], David A. Shapiro [3], Patrick Herring [4], Abraham Anapolsky [4], William C. Chueh [2,*], Colin Ophus [1], Andrew M. Minor [1,5,*]

[1] National Center for Electron Microscopy, Molecular Foundry, Lawrence Berkeley National Laboratory, Berkeley, CA 94708, USA
[2] Depart. of Mat. Sci. & Eng., Stanford University, Stanford, CA 94305, USA
[3] Advanced Light Source, Lawrence Berkeley National Laboratory, Berkeley, CA 94720, USA
[4] Toyota Research Institute, Los Altos, CA 94022, USA
[5] Depart. of Mat. Sci. & Eng., University of California, Berkeley, CA 94720, USA

Lithium iron phosphate (Li$_x$FePO$_4$), a cathode material used in rechargeable Li-ion batteries, phase separates upon de/lithiation under equilibrium. The interfacial structure and chemistry within these cathode materials affects Li-ion transport, and therefore battery performance. Correlative imaging of Li$_x$FePO$_4$ was performed using four-dimensional scanning transmission electron microscopy (4D-STEM), scanning transmission X-ray microscopy (STXM), and X-ray ptychography in order to analyze the local structure and chemistry of the same particle set. Over 50,000 diffraction patterns from 10 particles provided measurements of both structure and chemistry at a nanoscale spatial resolution (16.6–49.5 nm) over wide (several micron) fields-of-view with statistical robustness. Li$_x$FePO$_4$ particles at varying stages of delithiation were measured to examine the evolution of structure and chemistry as a function of delithiation. In lithiated and delithiated particles, local variations were observed in the degree of lithiation even while local lattice structures remained comparatively constant, and calculation of linear coefficients of chemical expansion suggest pinning of the lattice structures in these populations. Partially delithiated particles displayed broadly core–shell-like structures, however, with highly variable behavior both locally and per individual particle that exhibited distinctive intermediate regions at the interface between phases, and pockets within the lithiated core that correspond to FePO$_4$ in structure and chemistry. The results provide insight into the Li$_x$FePO$_4$ system, subtleties in the scope and applicability of Vegard's law (linear lattice parameter-composition behavior) under local versus global measurements, and demonstrate a powerful new combination of experimental and analytical modalities for bridging the crucial gap between local and statistical characterization.

Keywords: Batteries; Electron microscopy; X-ray Ptychography; 4D-STEM

* Corresponding authors.
  E-mail addresses: Hughes, L.A. (lauren.an.hughes@gmail.com), Chueh, W.C. (wchueh@stanford.edu), Minor, A.M. (aminor@lbl.gov).
# These authors contributed equally.

Introduction

Lithium iron phosphate (Li_xFePO_4) is a viable commercial cathode material for lithium (Li) batteries used in portable electronic devices and zero-emission vehicles due its high rate performance, good cycle life, and low cost [1,2]. However, mechanisms that affect Li-ion transport, which plays a dominant role in rate performance and cycle life, are not fully understood in Li_xFePO_4 [3–5]. A key question is how exactly the structure and chemistry of Li_xFePO_4 change as it phase separates into Li-rich ($LiFePO_4$) and Li-poor ($FePO_4$) phase domains [6–8]. To fully understand the functional behavior of Li_xFePO_4, the chemical reactions and phase transformations that occur upon de/lithiation must be clearly determined.

A multitude of microscopy techniques have been applied to analyze the Li distribution and crystallographic information of Li_xFePO_4 particles in order to determine the insertion/desertion mechanisms during cycling [9]. Scanning transmission X-ray microscopy (STXM) as well as X-ray ptychography have previously shown the distribution of Li during de/lithiation [10]. Chueh et al. show the effect of Li surface diffusion on phase transformation behavior of Li_xFePO_4 platelets via STXM [8]. They also show the incoherent nanodomains within Li_xFePO_4 ellipsoidal nanoparticles behave as distinct particles during delithiation via X-ray ptychography [11]. High resolution transmission electron microscopy (HRTEM) and selected area electron diffraction (SAED) have isolated defect concentration and crystallographic information (lattice parameters, strain, orientation) in $LiFePO_4$ and $FePO_4$ [12–14]. Electron energy loss spectroscopy (EELS) of the Fe-$L_{2,3}$ and O-K edges, as well as Li-K edge using low loss EELS, have revealed variations in electronic bonding configuration and Li concentration at the interface in which these two phases interact [15–17]. Annular bright field (ABF) imaging has captured changes in local atomic structure and Li-ion location at the phase separated interface within Li_xFePO_4 platelets [18,19]. While these microscopy techniques successfully highlight structural and chemical changes at the phase separated interfaces within de/lithiated Li_xFePO_4, they did not correlate both structure and chemistry globally and locally within the same particles as their field of view was limited to selected regions of interest. Restrictions within these characterization techniques, due to sample thickness and statistics, have led to discrepancies between the experimental observations and the proposed theoretical models regarding the mechanisms of de/lithiation within Li_xFePO_4 [17,20].

In regards to analyzing structural effects, automated crystal orientation mapping (ACOM) in TEM in combination with energy filtered TEM (EFTEM) has also been used to analyze phase transformation behavior in $LiFePO_4$, providing some statistical information on crystal orientation and structure [21,22]. For this technique, the experimental electron diffraction patterns are compared to a database of simulated diffraction templates calculated from literature. $LiFePO_4$ and $FePO_4$ are both orthorhombic with space group *Pnma* [13,23] and reported crystalline lattice parameters of a = 10.33 Å, b = 6.01 Å, c = 4.69 Å for $LiFePO_4$, and a = 9.81 Å, b = 5.79 Å, c = 4.78 Å for $FePO_4$, respectively [13,23]. However, the crystal structure and lattice parameters

for potential intermediate phases are unknown due to phase separation; simulated datasets must then make assumptions regarding any possible intermediate phases. For example, an intermediate phase within cycled Li_xFePO_4 is assumed to be a solid solution of $LiFePO_4$ and $FePO_4$ in which 50% of the sites are occupied by Li and the lattice parameters are an average of the lattice parameters of $LiFePO_4$ and $FePO_4$ phases [22]. Phase mapping over micrometers at nanometer resolution is therefore possible with ACOM-TEM, but the assumptions required to make the method viable may obscure novel or unexpected structures within de/lithiated Li_xFePO_4 such as new phases or any nonlinearity in lattice parameter variation with composition.

In previous work, the study of phase distribution within Li_xFePO_4 as a function of de/lithiation has been performed separately via diffraction, spectroscopy, or X-ray techniques [11,24,25]. However, to accurately delineate the structural and chemical transformations as well as their relationship to one another, the data acquired from diffraction and spectroscopy techniques must be directly comparable and statistically applicable [21,26–28]. Therefore, in this correlative study, four-dimensional scanning transmission electron microscopy (4D-STEM) and two X-ray microscopy techniques, STXM and X-ray ptychography, were performed on the same Li_xFePO_4 platelets. This combination allows for pixel-by-pixel correlation of the datasets, such that the lattice parameters and lithium content can be extracted and compared over fields-of-view, which span complete particles with statistical robustness, and was not previously achievable due to technique and data acquisition limitations. In our study, ten particles were examined – three lithiated, five partially delithiated, and two delithiated – comprising over 50,000 diffraction patterns. Due to data-size and electron beam damage constraints, all ten particles were initially measured by 4D-STEM with a comparatively large step-size of 49.5 nm between collected diffraction patterns. A single partially delithiated particle was then examined in finer detail with a step-size of 16.6 nm. In each case, the electron and X-ray data were used to extract the lattice parameters and percent lithiation, and the results were correlated to allow for direct, local comparison. The results show local variations, which likely would be lost under either broad-beam characterization or traditional high resolution, but narrow field, microscopy. In a separate publication using this data, inverse learning of the chemomechanics is performed and a variety of models are subsequently analyzed [29]. Thus, the acquired correlative imaging results demonstrate the capabilities of 4D-STEM combined with STXM/X-ray ptychography for isolation and identification of structural variations, which is a necessary component for the development of insertion/desertion kinetic modeling of Li_xFePO_4.

Within this work, the Li_xFePO_4 particles are categorized by three chemical ranges based on the average Li composition (x) of each particle: $0 \leq x \leq 0.15$ is defined as FP, $0.15 < x \leq 0.85$ is defined as L_xFP, $0.85 \leq x \leq 1$ is defined as LFP. When discussing literature values or comparing to the 'pure' bulk phase, $LiFePO_4$ or $FePO_4$ are used. Li_xFePO_4 is a catchall for all compositions.
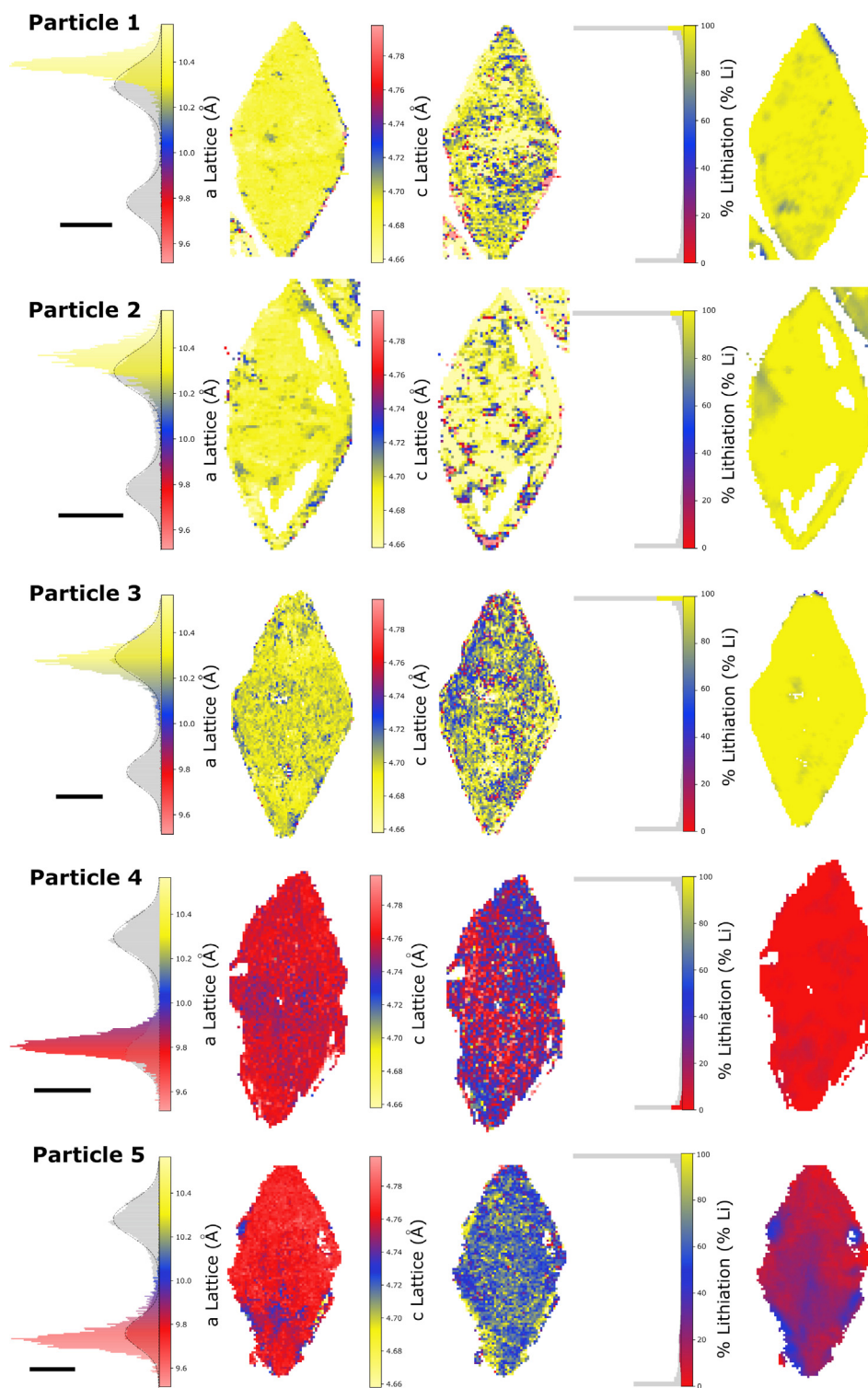
FIGURE 1

Pixel-by-pixel correlation of Li$_x$FePO$_4$ particles: The a-lattice parameter map, the c-lattice parameter map, and % lithiation map for LFP (Particles 1–3), FP (Particles 4–5), L$_x$FP (Particles 6–9). The color scheme is the same: red denotes regions that have chemistry or lattice parameters that correspond to FePO$_4$, yellow denotes regions that have chemistry or lattice parameters that correspond to LiFePO$_4$, blue denotes regions that have chemistry and lattice parameters that correspond to their mean. The lithium composition was determined using STXM for LFP and FP particles, and X-ray ptychography for L$_x$FP. The step-size used for the 4D-STEM measurements was 49.5 nm. Definition of the colormaps is discussed further in the Supplemental Materials.
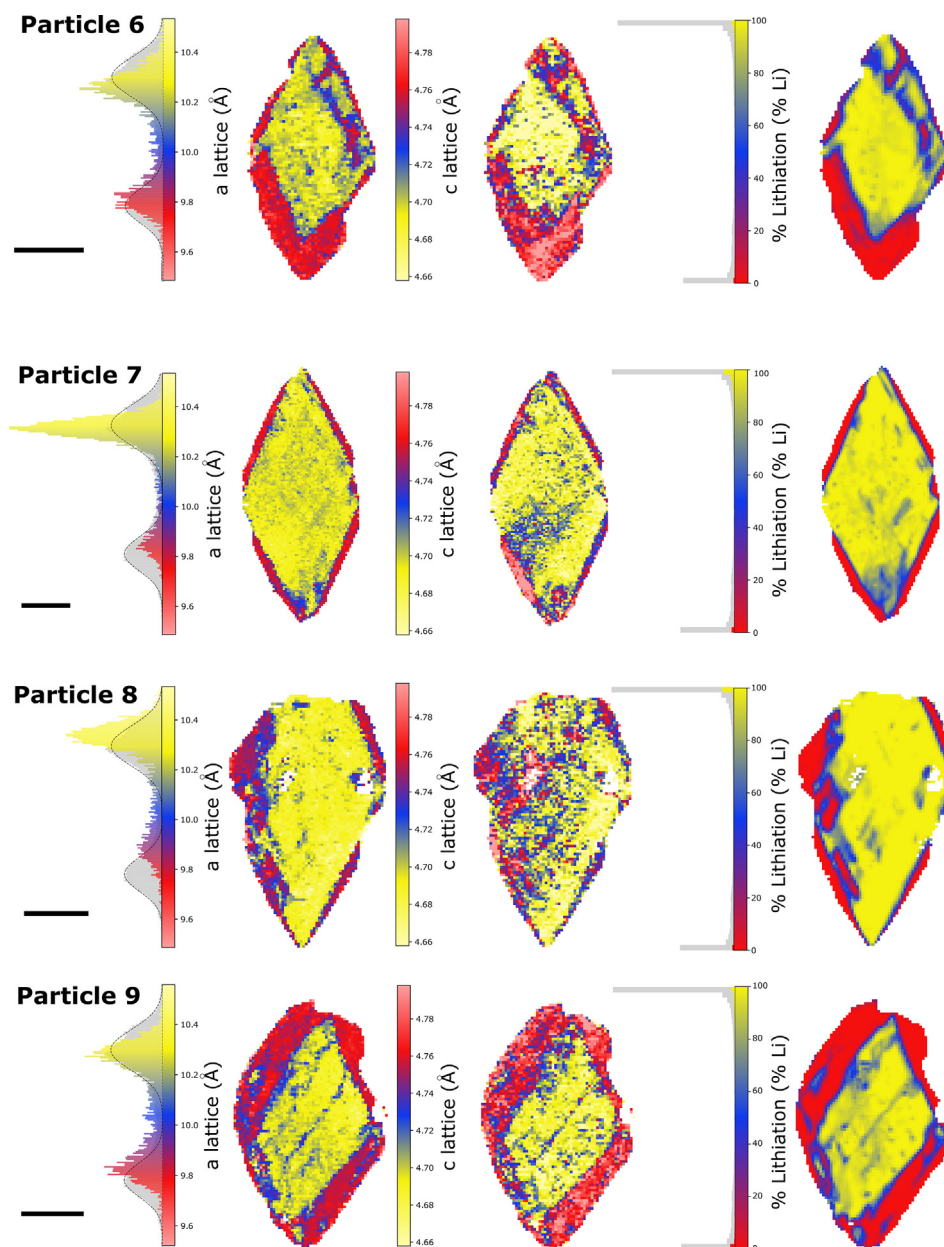
Fig. 1 (*continued*)

Results

Pixel-by-pixel correlation of Li$_x$FePO$_4$ particles using 4D-STEM and X-ray microscopy

Fig. 1 shows a- and c-lattice parameter maps and chemical composition maps for nine Li$_x$FePO4 platelets. For these maps, red denotes values of each parameter (a- and c- lattice parameters as well as chemical composition) corresponding to FePO$_4$; yellow denotes values corresponding to LiFePO$_4$; and blue denotes intermediate values. These plots were produced by first performing 4D-STEM with a 49.5 nm step-size and then performing STXM or X-ray ptychography on the exact same Li$_x$FePO$_4$ particles, with each platelet aligned along the [010] direction. A single crystallographic orientation was observed for each platelet. Lattice parameters were extracted by fitting the Bragg scattering within each 4D-STEM diffraction pattern (see Methods and Supplemen-

tal Material) [30]. Chemical composition values were determined using the X-ray signal obtained from 5 different energy slits about the Fe-K edge (Methods and Supplemental Material). Correlative analysis produced additional information such as HAADF-STEM, X-ray optical density, and shear and rotational strain for each particle. Pixel-by-pixel correlation between the X-ray and 4D-STEM signals was performed using an affine transformation optimized by gradient descent (see Methods and Supplemental Material). Sixteen distinct image-like information channels were ultimately extracted for each particle (see Supplemental Material). While we focus primarily on the a-lattice, c-lattice, and percent lithiation channels in this work, this data is highly information rich – for instance, the HAADF-STEM and X-ray optical density images for all the Li$_x$FePO$_4$ particles show the presence of internal voids of varying size and shape. We
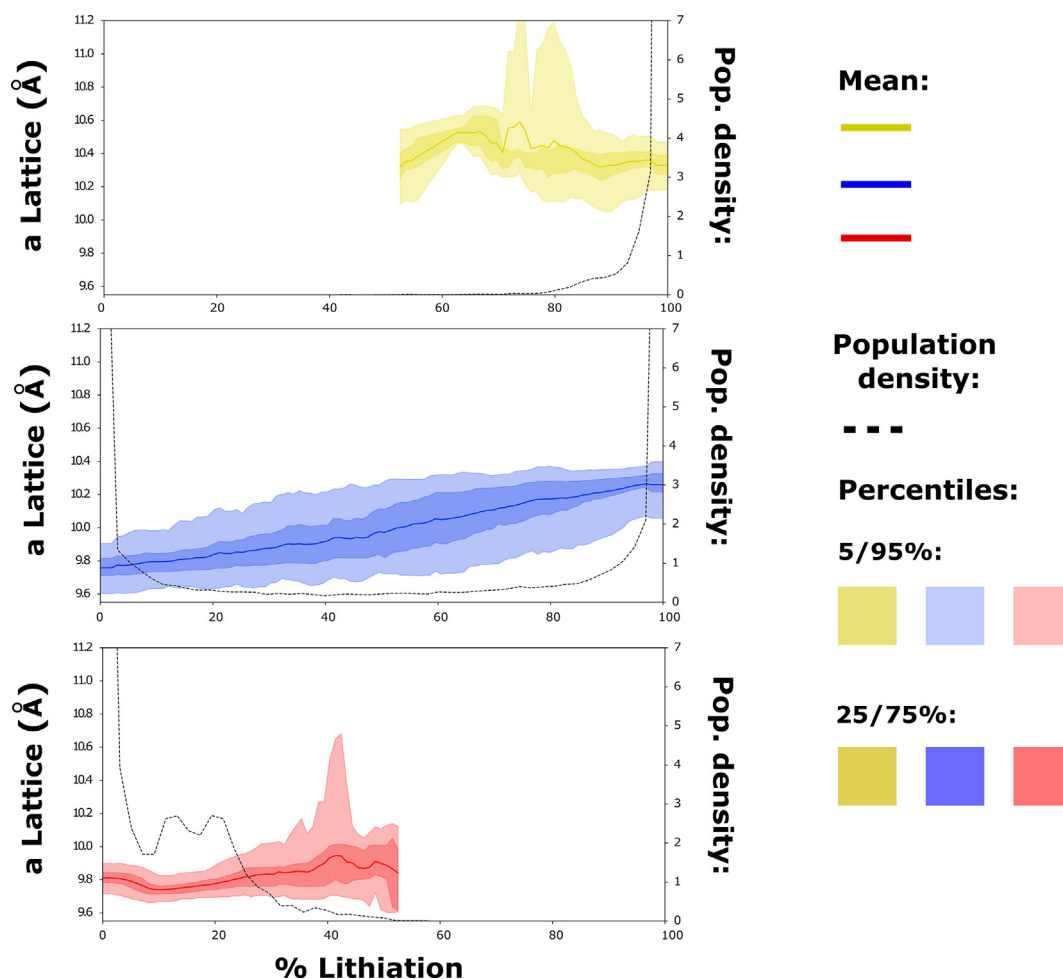
FIGURE 2

Population density, mean, and percentile for all Li_xFePO_4 particles: changes in the a-lattice parameter compared to % lithiation for (a) all LFP particles, (b) all L_xFP particles, and (c) all FP particles.

therefore made this data freely and publicly available for further study – see Data Availability.

From the Li-composition-distribution maps, LFP platelets are shown to be fully lithiated with minimal fluctuation in Li content regardless of internal void structure (Particles 1, 2, and 3 in Fig. 1). We measure both a- and c-lattice parameter values that are consistent with the literature, finding $a = 10.33 \pm 0.13$ Å and $c = 4.69 \pm 0.05$ Å, where the error terms quoted here represents the standard deviation of the distribution. The noisier appearance of the c-lattice parameter maps in Fig. 1 compared to the a-lattice parameter is likely due to the fact that, for the a-lattice parameter, the two peaks of bimodal distribution are cleanly separated; while for the c-lattice parameter, the two peaks of bimodal distribution are not distinctly separated. This difference in bimodal distribution is discussed further in the analysis of the singular L_xFP particle within the next section. Overall, the experimental LFP platelets, from 4D-STEM and STXM analysis, demonstrate lattice parameters and chemistry that correspond well with literature [1].

The Li composition-distribution maps of FP platelets, in contrast, demonstrate that these platelets are not fully delithiated. Particle 5 shows a modest fluctuation of Li content, resulting in

purple-blue regions throughout the overall platelet; while Particle 4 shows uniform, minimal Li content (Fig. 1). Interestingly, the a-lattice parameter map for Particle 5 exhibits small, concentrated clusters with intermediate a-lattice parameter values, approximately 10.0 Å. These clusters overlap with fluctuations in the Li concentration. However, the variation within the Li concentration is more diffuse throughout the FP platelet as the platelet shows a Li concentration gradient change from the fully delithiated regions to the intermediate lithiated regions, whereas the intermediate a-lattice parameter values are distinct from the fully delithiated regions, i.e., color gradation within the a-lattice parameter map for Particle 5 does not directly correspond to the color gradation of the Li composition map. The c-lattice parameter maps for FP, similar to LFP particles, show intermediate lattice parameter values, which fall within the literature range [1,13]. Modest fluctuation of Li within delithiated FP can be attributed to a number of factors related to defect concentration, surface morphology, and lithiation pathways that are all sample dependent [31].

The L_xFP platelets, overall, show a Li-rich core and Li-poor outer shell (Particles 6–9 in Fig. 1). In the delithiated (lithiated) regions, we find an a-lattice parameter of 9.82 ± 0.16 Å ($10.22 \pm$

0.15 Å) using mean statistics, and a value of 9.76 ± 0.16 Å (10. 28 ± 0.15 Å) with median statistics, where in both cases the error term is the standard deviation. Similarly, for the c-lattice parameter we find 4.76 ± 0.03 Å (4.70 ± 0.03 Å) in the means and 4.7 7 ± 0.03 Å (4.69 ± 0.03 Å) in the medians. In terms of percentage contraction/expansion from the lithiated to the delithiated regions, the a-lattice is found to contract by 3.9% in the means and 5.1% in the medians. The c-lattice is found to expand by 1.3% in the means and 1.7% in the medians. The mean and median statistics vary meaningfully here due to distributions with meaningful skewness, and the full distributions can be found in the Supplemental Material. In comparison to the values reported by Zhang when Li-ions were extracted from Li_xFePO_4, we find similar c-expansion values to theirs (1.9%), and our a-contraction values are somewhat less than their report (6.77%) [1].

The interface between the Li-rich core and Li-poor shell of the L_xFP platelets show intermediate a-lattice parameter values and Li composition, which is highlighted in blue within these maps. Each L_xFP particle (Particles 6–9) exhibits a different, non-uniform core–shell behavior, in which there is not a stark separation of the Li-rich and Li-poor domains, e.g., there are Li-poor pockets within the lithiated core and there are partially lithiated pockets within the delithiated outer shell. Some partially lithiated and fully delithiated pockets are correlated with the presence of voids. For instance, a partially delithiated region, denoted in blue, at the base of L_xFP Particle 7 follows the shape

of the connected void structures observed in both the HAADF-STEM and X-ray optical density images shown in the Supplemental Material. However, a clear relationship between composition and void structure is not observed for all the particles. We explore this relationship between local structure and Li chemistry in a following section.

Structure-composition relationship for all Li_xFePO_4 particles

Vegard's law predicts that in a solid solution of two materials, the lattice parameters will scale linearly with the weighted mean of those two constituents, i.e., linear lattice parameter-composition behavior is observed within a uniform, stress-free state. In Fig. 2, the a-lattice parameter as a function of lithiation for all the LFP, L_xFP, and FP particles is plotted.

For the LFP and the FP particles, the a-lattice parameter is shown to be consistent with bulk phase $LiFePO_4$ or $FePO_4$, respectively, regardless of changes in lithiation (Fig. 2a and c). This apparent pinning of the a-lattice parameter indicates the mean behavior of these particles does not always follow Vegard's law. The population density curves (dashed lines) show the vast majority of counts are fully lithiated/delithiated in the LFP/FP, dropping rapidly for lithiations below 90% in LFP and above 10% in FP. Mechanistically, we therefore surmise this pinning of the a-lattice parameter with respect to % lithiation may be caused by the predominantly 'pure' LFP or FP crystal structures preventing lattice relaxation in the relatively small and few regions of partial lithiation.

In contrast, Fig. 2b shows Vegard's law is, on average, obeyed in the L_xFP particles. The mean of the a-lattice parameter is shown to vary linearly with the Li content. We reiterate, however, that these measurements are spatially averaged, which masks any local variability and is therefore a significant qualifier when drawing conclusions regarding structure-composition behavior of de/lithiated Li_xFePO_4.

To quantify this analysis, we computed the linear coefficients of chemical expansion, shown in Table 1. We computed linear fits to the a- and c- lattice parameters versus lithiation distributions for each particle, then found the mean and standard deviations above using all particles at a given lithiation. The L_xFP α values are fully consistent with bulk measurements, while the
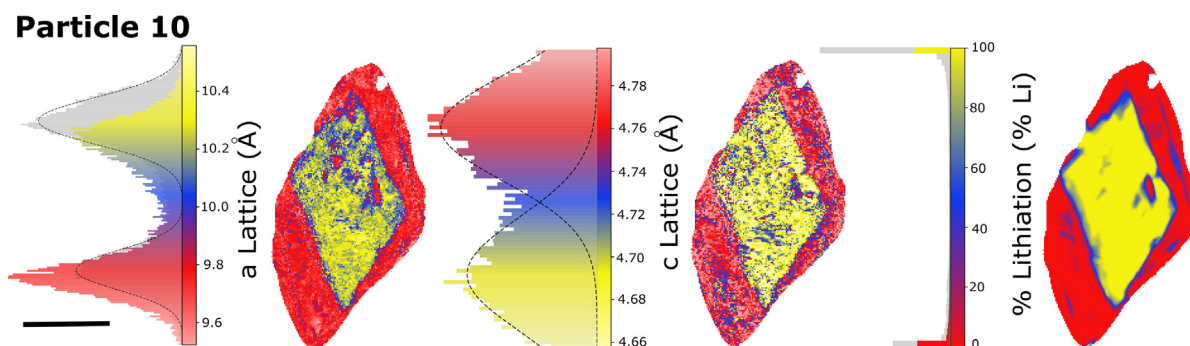
TABLE 1

Chemical expansion coefficients of LxFP: The linear coefficients describing the statistical expansion of the a- and c- lattice parameters (α_a and α_c) with lithiation.

Type	α_a (Å/%Li)	α_c (Å/%Li)
LFP	−0.033 ± 0.219	0.062 ± 0.079
L_xFP	0.502 ± 0.025	−0.073 ± 0.016
FP	0.174 ± 0.291	−0.046 ± 0.017
Lit.	0.524	−0.089

FIGURE 3

Pixel-by-pixel correlation of L_xFP: (a) a-lattice parameter map, (b) the c-lattice parameter map, (c) % lithiation map. For lattice parameter and lithium composition-distribution maps, the color scheme is the same as Fig. 1. The a- and c-lattice parameter and % lithiation maps also have corresponding histograms in which the grey-scale histogram corresponds to all the data taken from the ten particles and the color-scale histogram corresponds the data acquired from the individual particle.

FP/LFP α values are much smaller, and within an experimental error of zero, i.e. the lattice parameters are pinned. Notably, however, the error for the FP/LFP values is comparatively large, a reflection of the small population densities of pixels at intermediate lithiations within the fully de/lithiated particles. See Supplemental Information for more detailed information.

Detailed analysis of a single L_xFP particle

A higher-resolution 4D-STEM dataset of L_xFP was also acquired with a smaller step-size of 16.6 nm (Particle 10, Fig. 3). In Fig. 3, pixel-by-pixel correlated maps of the a- and c- lattice parameters and Li composition were generated via 4D-STEM and X-ray ptychography. The phase separation interface between the Li-rich core and the Li-poor shell of the 16.6 nm step-size map shows intermediate a-lattice parameters and Li chemical compositions, denoted in blue, similar to the interfaces observed in the 49.5 nm step-size L_xFP maps (Particles 6–9, Fig. 1).

The histograms associated with each map show the populations of the relevant platelet quantities. The grey-scale histograms are populations derived from the data of all ten particles, while the color-scale histograms use the data of only Particle 10. The dashed lines show the pair of best-fit gaussians to the whole-population distributions. If the fit gaussians are taken as representative of the "pure" phase parameter distributions, it is apparent the a-lattice parameter histogram consists of two distinct, well segmented lobes with non-overlapping tails. Yet, this particle contains a statistically significant number of counts in between the two lobes and above the gaussian tails, and in the associated map it is apparent these counts arise primarily at and near the phase separation interfaces (blue regions). Thus, there exists narrow, but well-defined regions, which are structurally distinct from the pure phases. In contrast, the histogram of the c-lattice parameter is bimodal, but there is significant overlap between the lobes of the distribution associated with the fully lithiated and fully delithiated regions (Fig. 3b). This phenomenology is related to the comparatively small median c-lattice parameter expansion of 1.7% compared to the 5.1% contraction of the a-lattice parameter, which causes difficulty in statistically distinguishing a separation between the two phases by the c-lattice parameter values as noted elsewhere in the literature [13]. We also note that this overlap between the normal distribution of the LFP and FP regions for the c-lattice parameter, and the comparative size scales spanned by the color bars for the a- and c-lattice parameters, are likely the cause of the signal to noise difference between the two structure maps.

In the analysis of L_xFP for Fig. 2b, the a-lattice parameters were found to scale linearly with Li content after spatial averaging and a perspective of the overall structure-chemistry behavior was gained for these particles. However, 4D-STEM in combination with X-ray ptychography allows for analysis of the fine structural variations along with the average bulk variations within a particle. From the perspective of Fig. 3, there are two interesting local structure-chemistry features. Firstly, within the Li-rich core of the L_xFP Particle 10, there is a contained pocket in which the a- and c-lattice parameters and Li content corresponds to the $FePO_4$ phase. This delithiated pocket is consistent with the location of a void observed in the HAADF-STEM and X-ray optical density images (see Methods and Supplemental Material). Secondly,

within the Li-poor shell of the L_xFP Particle 10, there are regions which show intermediate a- and c- lattice parameters with partial delithiation. These intermediate regions mimic the line and shape of the phase separation interface and may thereby indicate the movement of the phase separation interface within the particle during the delithiation process.

Error analysis and statistics in L_xFP particle 10

The particles examined were $\sim$ 300–400 nm thick and non-uniform in thickness. This sample thickness creates significant challenges in analysis via the electron beam due to multiple scattering effects [32]. Thinner samples are preferable from a characterization perspective, though not always possible with real-world samples. The size of particles can alter their qualitative behaviors; and, in this instance, platelets with the best figure of merit for function, such as electrochemical cycling, are thick to an electron beam. In these cases, error analysis is essential to understand the realm of validity of any quantitative analysis.

Here we performed cross validation to calculate a root mean square error (RMSE) associated with the fit lattice vectors at each scan position. Briefly, this process involved fitting the lattice vectors to a subset of the detected Bragg peaks at each scan position, then computing how much the remaining subset of peaks deviated from their predicted position given these lattice vectors. The result is a pixelwise map of RMSE, shown in Fig. 4a. More details, and discussion of why this approach is preferable to quoting the lattice fitting error, are in Supplemental Material. We found the majority of the lattice vectors fits to be trustworthy, but there are several regions of high RMSE in which results are suspect. Thresholding the RMSE image to generate a mask gives the green region within Fig. 4e. Examining the diffraction patterns provides insight into why the error is increased within these regions. Fig. 4m shows the average of 30 diffraction patterns from a selected high RMSE region (shown in green in Fig. 4f), which has an extremely low signal-to-noise ratio and no diffraction spots are visible to the eye. In general, we find the high RMSE regions fall into three categories: (1) very low SNR, (2) most detected Bragg peaks are colinear, or (3) redistribution of intensity inside the disks near the particle edges. The low SNR diffraction patterns typically appear to be due to sample thickness, additional material agglomerated on the particle, or local lattice tilt. See the Supplemental Material for further discussion. Most crucially, careful assessment of the CV error reveals that, in spite of the large sample thickness, the fit lattice vectors are trustworthy for the vast majority of pixels, suggesting the validity of the subsequent analysis.

We also computed local deviation from Vegard's law. Our metric δ is given by $\delta = a - a_{FP} - \%Li(a_{LFP} - a_{FP})$ and represents the deviation, in units of length, of the local a-lattice parameter from the value predicted by Vegard's law. In Particle 10, we found several pockets of anomalous contraction of a-lattice parameter in the upper area of the lithiated core, colored in red in Fig. 4b. Comparing this contraction directly to the measured Li content (Fig. 4c and e), there is no local change in Li and the regions are nominally fully lithiated. To understand if this anomalous contraction represents a real change to the lattice, we then isolated these regions, using a threshold to generate a mask, shown in blue in Fig. 4e. An average of 30 diffraction pat-
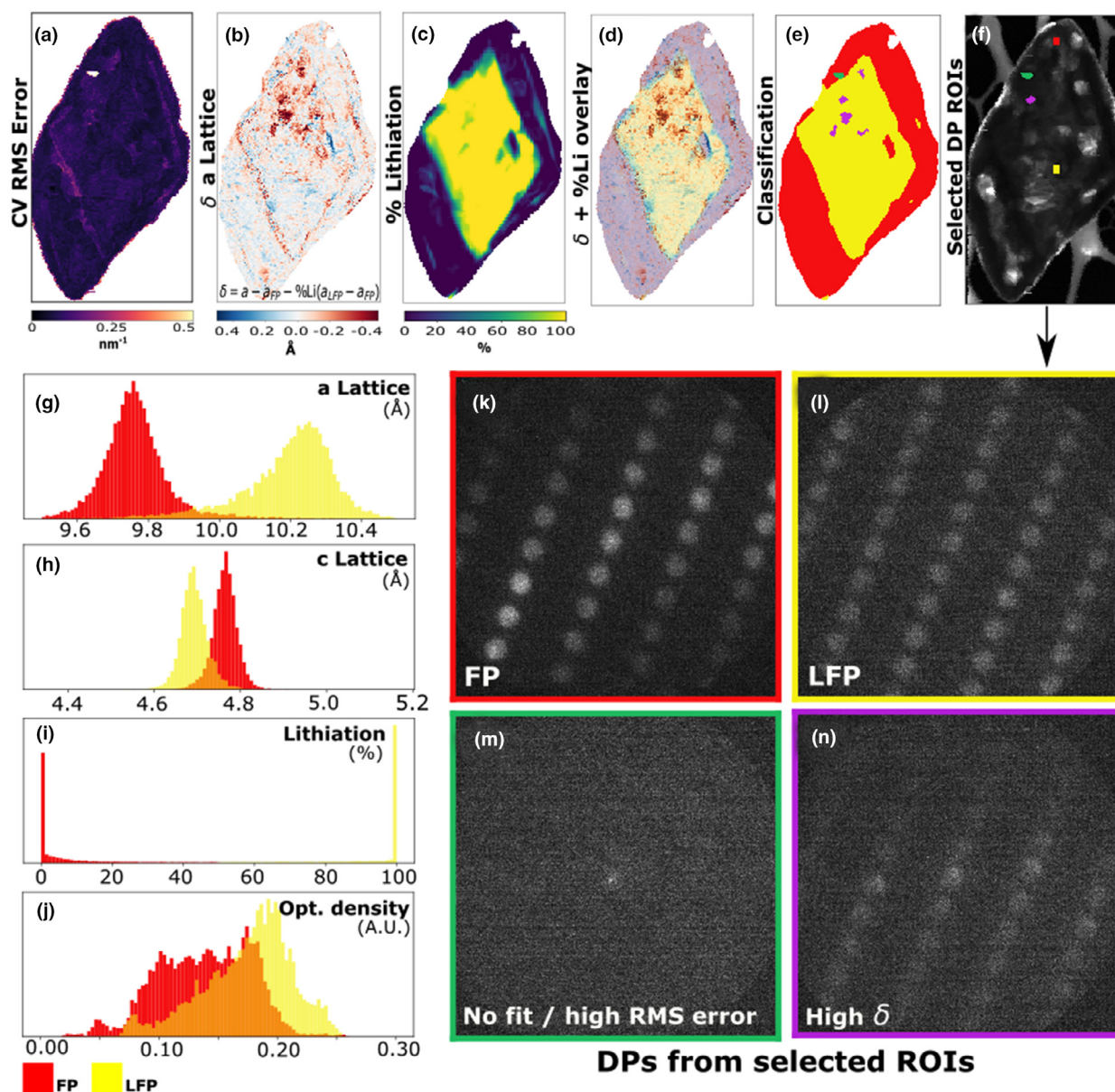
FIGURE 4

Error analysis and segmentation of L_xFP Particle 10: (a) A map showing cross validation root mean square error associated with the measured lattice vectors at each pixel; (b) the deviation in the a-lattice parameter at each pixel relative to the values expected using Vegard's law in combination with the experimental, bulk FP and LFP values; (c) % lithiation of L_xFP Particle 10; (d) an overlay of the changes in a-lattice parameter at each pixel and the % lithiation map; (e) a segmentation of regions of statistically significant a-lattice parameter deviation from Vegard's law (blue) and RMS error (green) as compared to bulk LFP (yellow) and FP (red); (f) ADF image with colorized size-limited regions of these four segments (FP, LFP, deviation of Vegard's, and RMS error with their corresponding diffraction patterns (k-n)). Histograms of the (g) a-lattice parameter, (h) c-lattice parameter, (i) % lithiation and (j) thickness values of Li_xFePO_4 Particle 10, where red/yellow indicate FP/LFP, and overlap between the two histograms curves is in orange.

terns from this region is shown in Fig. 4n. We found that, while these regions had a sufficiently high SNR to detect Bragg scattering, the disks themselves were smeared, indicating possibly a tilt of the lattice or overlapping structures, preventing conclusive measurement of the a-lattice parameter in these regions. In light of these considerations we estimated the systematic error associated with our measured lattice parameters and found a systematic error associated with the a-lattice of 3.6 ± 1.5 pm and with the c-lattice of 2.2 ± 1.8 pm. See the Supplemental Materials.

Using a cutoff at 50% lithiation, we segmented the remaining diffraction patterns into regions classified as FP and LFP, shown in red and yellow respectively in Fig. 4e. With these regions, we can then compute structural statistics based on local behavior while remaining confident in the validity of the measurements. Fig. 4k and l show images averaged over 30 diffraction patterns each from the FP and LFP regions shown in Fig. 4f. Circular Bragg disks with good SNR are visible by eye. Fig. 4g–j shows histograms of several parameters of interest for the two phases:

the a- and c- lattice parameters, the percent lithiation, and the optical density (a good proxy for thickness). The a- and c- lattice values show means consistent with the literature. The overlap of the tails of the distributions in the c-lattice parameter indicate that local variation is on similar order to the difference between c_{FP} and c_{LFP}, making the c-lattice value a poor metric for phase determination. The optical density tends to be higher in the LFP, which is sensible given the tendency of platelets to taper at their edges where the FP is located. Careful error analysis and masking of suspect diffraction patterns makes it possible to make these measurements with confidence.

Discussion

Excluding Particle 7, which has sharply defined edges and is the closest to a diamond shape, the remaining L_xFP platelets exhibit delithiated shells that are non-uniform (Particles 6–9, Fig. 1). Certain particle edges of the L_xFP delithiated more rapidly compared to other particle edges. This variation is likely due to changes in the surface energy of the linear edge compared to the rough or curved edge of these platelets, which then alters the rate of Li-ion diffusion [13,33,34]. The non-uniform platelet delithiation, the distinct and unevenly distributed phase-separation interfaces demonstrate the importance of these nanoscale resolution, micrometer-scale field-of-view, and statistically robust datasets. As we demonstrated within this work, the L_xFP particles show changes in structure and chemistry across a few nanometers distance as well as between particles.

Combining 4D-STEM and X-ray microscopy techniques allows for the multiscale analysis necessary for observing the structural and chemical changes in which Li_xFePO_4 and other battery materials undergo as a function of delithiation. This work suggests that Li_xFePO_4 platelets have a-lattice parameters values which do not follow the Vegard's law, i.e., linear lattice parameter-composition behavior, even under position averaging, in the FP and LFP states (Fig. 2); and that the L_xFP platelets show a statistically significant fraction of pixels that correspond to the intermediate values, which varies locally within particles and from particle to particle (Figs. 1 and 3). Thus, the results illustrate the significant variability of structure and chemistry within these particles and between differing particles, which undoubtedly affects analysis when data acquisition is confined to a narrow scope. Data acquisition which is confined solely to a narrow field of view (often associated with electron microscopy experiments) or a wide field of view but spatially averaged (often associated with X-ray microscopy experiments) can miss or overlook key components of analysis crucial to fundamentally understanding of battery materials [3,4,21].

In total, the datasets presented combined local nanoscale resolution across several micrometer fields of view, correlated structural and chemical channels, and the statistical robustness afforded by new "big data" experimental methods like 4D-STEM. With no assumptions regarding ascribed literature values or diffraction pattern templates, we calculated the lattice parameters and compositions directly from the raw data. The unique combination of local and statistical measurements enabled a more nuanced look into Vegard's law in this system: for fully lithiated/delithiated particles, a spatially-averaged description (Fig. 2) indicated deviations from Vegard's law, even while it was obeyed within the vast majority of local measurements (Fig. 1). In partially delithiated particles, Vegard's law was obeyed under spatial averaging (Fig. 2), while the local picture was more complex and not yet fully clear. These local and statistical measurements also identified intermediate structure-chemistry values at the phase separation interface, i.e. a- and c- lattice parameters as well as Li content in between the $FePO_4$ and $LiFePO_4$ phases (Figs. 3 and 4).

Conclusion

Ten Li_xFePO_4 platelets at different stages of chemical delithiation (lithiated LFP, L_xFP, and delithiated FP) were characterized using 4D-STEM, STXM, and X-ray ptychography. Our correlative microscopy approach allows for a pixel-by-pixel correlation and comparison of the structure and chemistry of Li_xFePO_4. From the acquired 4D-STEM and X-ray microscopy datasets, the a- and c- lattice parameter values and the Li concentration were calculated to determine the average and local structure-chemistry relationship. We observe that, on average, the L_xFP platelets follow Vegard's law, in which the changes in structure and chemistry are directly correlated. Thus, this correlative technique using 4D-STEM and X-ray microscopy independently calculates the structure and chemistry of μm-size platelets at nm-resolution from raw data and provides a methodology for sample analysis that encompasses robust statistics, high spatial resolution, a particle-size field of view, and minimal assumptions regarding material characteristics and properties.

Declaration of Competing Interest

The authors declare that they have no known competing financial interests or personal relationships that could have appeared to influence the work reported in this paper.

Acknowledgements

Contributions

H.D.D., N.J., and E.L. synthesized and prepared the samples. H.D.D. and N.J. performed STXM and ptychography experiments. Y.-S.Y. and D.A.S. assisted in the STXM and ptychography experiments. H.D.D. analyzed the STXM and X-ray spectro-ptychography data. L.A.H. performed the 4D-STEM experiments. L.A.H. and B.H.S. analyzed 4D-STEM data. C.O. performed the image registration. L.A.H. prepared the initial draft of the manuscript. All authors contributed to the discussion of the results and writing of the manuscript. W.C and A.M.M supervised the project.

Data availability

The 4D-STEM and X-ray microscopy data associated with this manuscript can be found at: https://data.matr.io/6/.

Appendix A. Supplementary data

Supplementary data to this article can be found online at https://doi.org/10.1016/j.mattod.2021.10.031.

References

[1] W.J. Zhang, J. Power Sources 196 (6) (2011) 2962–2970.
[2] L.X. Yuan et al., Energy Environ. Sci. 4 (2) (2011) 269–284.
[3] R. Malik, A. Abdellahi, G. Ceder, J. Electrochem. Soc. 160 (5) (2013) A3179–A3197.
[4] F. Yu et al., RSC Adv. 4 (97) (2014) 54576–54602.
[5] C.T. Love et al., J. Electrochem. Soc. 160 (5) (2013) A3153–A3161.
[6] W. Lv et al., Appl. Phys. Lett. 108 (2016) 083901.
[7] N. Meethong et al., Adv. Funct. Mater. 17 (2007) 1115–1123.
[8] Y. Li et al., Nat. Mater. 17 (2018) 915–922.
[9] S. Kobayashi et al., Nat. Commun. 9 (2018) 1–10.
[10] N. Ohmer et al., Nat. Commun. 6 (2015) 6045.
[11] Y. Li et al., Adv. Mater. 27 (2015) 6591–6597.
[12] H. Gabrisch, J. Wilcox, M.M. Doeff, Electrochem. Solid-State Lett. 11 (2008) A25–A29.
[13] C.V. Ramana et al., J. Power Sources 187 (2) (2009) 555–564.
[14] G. Chen, X. Song, T.J. Richardson, Electrochem. Solid-State Lett. 9 (2006) A295–A298.
[15] L. Laffont et al., Chem. Mater. 18 (2006) 5520–5529.
[16] W. Sigle et al., Electrochem. Solid State Lett. 12 (2009).
[17] M.E. Schuster et al., Chem. Mater. 26 (2014) 1040–1047.
[18] L. Gu et al., J. Am. Chem. Soc. 133 (2011) 4661–4663.
[19] C. Zhu et al., Adv. Funct. Mater. 24 (2014) 312–318.
[20] D.A. Cogswell, M.Z. Bazant, Electrochem. commun. 95 (2018) 33–37.
[21] X. Mu et al., Ultramicroscopy 170 (2016) 10–18.
[22] G. Brunetti et al., Chem. Mater. 23 (2011) 4515–4524.
[23] A.S. Andersson et al., Solid State Ionics 130 (2000) 41–52.
[24] C. Delmas et al., Nat. Mater. 7 (2008) 665–671.
[25] P. Moreau et al., Appl. Phys. Lett. 94 (2009) 123111.
[26] C. Delmas, et al., Lithium deintercalation in LiFePO4 nanoparticles via a domino-cascade model, in: *Materials for Sustainable Energy: A Collection of Peer-Reviewed Research and Review Articles from Nature Publishing Group* 180–186 (World Scientific Publishing Co., 2010). doi:10.1142/9789814317665_0025.
[27] D. Robert et al., ACS Nano 7 (12) (2013) 10887–10894.
[28] M. Herbig, P. Choi, D. Raabe, Ultramicroscopy 153 (2015) 32–39.
[29] H.D. Deng, et al. Inverse learning of chemo-mechanics in LiXFePO4 from correlative X-ray and electron microscopy. (2021) http://arxiv.org/abs/2107.06192.
[30] B.H. Savitzky et al., Microsc. Microanal. 27 (4) (2021) 712–743, https://doi.org/10.1017/S1431927621000477.
[31] Y. Li et al., Adv. Funct. Mater. 25 (2015) 3677–3687.
[32] D.B. Williams, C.B. Carter, in: Transmission Electron Microscopy, Springer US, Boston, MA, 1996, pp. 3–17, https://doi.org/10.1007/978-1-4757-2519-3_1.
[33] L. Wang et al., Phys. Rev. B 76 (2007) 165435.
[34] K. Weichert et al., J. Am. Chem. Soc. 134 (2012) 2988–2992.